Institute of Solid State Physics

Project Thesis

Infrared spectroscopy of Fe_2VAl and $Fe_2V_{0.8}W_{0.2}Al$ compounds

Supervisor: Dr.phil. Evan Constable, Dipl.-Ing. Lorenz Bergen and Dr.rer.nat. Andrei Pimenov

Sahra Black
matriculation number: 01425259

Vienna, April 29, 2021

1 Abstract

Thermoelectric materials have attracted much interest in recent years for their ability to convert a thermal gradient into an electric current, thereby acting as an electric power generator. Full and half Heusler compounds have attracted special interest in the growing field of thermoelectricity for several members with a high thermoelectric performance. One Heusler compound in particular Fe_2VAl was under investigation for its high power Factor PF and its high thermoelectric figure of merit ZT. [1]

Recently the element doped thin film $Fe_2V_{0.8}W_{0.2}Al$ broke the world record for the highest thermoelectric figure of merit, ZT of roughly 5 ever recorded. [2]

With the drastic change in climate due to the rise of greenhouse gases in the atmosphere, environmentally friendly energy technologies are becoming more important than ever. Thermoelectric materials offer a low cost green energy solution for harvesting and recovering heat and converting it into electricity. This is especially important to recycle wasted heat in a variety of industries. [3]

Engineering new materials with a high thermoelectric figure of merit ZT is therefore an important goal in combating climate change. Investigating the microscopic electronic behavior aids the understanding of the thermoelectric figure of merit ZT and thereby might lead to new discoveries of improving it.

In this project thesis the dielectric response of the thermoelectric materials Fe_2VAl and $Fe_2V_{0.8}W_{0.2}Al$ were investigated with the usage of Fourier-transformed infrared (FTIR) spectroscopy. This led to a better understanding of the different contribution to to the thermoelectric figure of merit ZT.

Contents

2 Theoretical background

2.1 Thermoelectric performance

Knowing the maximum efficiency η_{max} of a thermoelectric material as an upper bound of its performance aids in identifying the underlying processes in the material. It can be derived by looking at the thermoelectric effects in a thermoelectric generator and counting the amount of power which is introduced to the system $\dot{Q}_{in}$ and the amount of power which comes out $P_{e,out}$ of the system.

$$\eta = \frac{P_{e,out}}{\dot{Q}_{in}} \tag{2.1}$$

A thermoelectric generator consists of a p-type and an n-type rod connected by a metallic bridge. This intermetallic bridge has a temperature of T_H. The p-type rod has a positive Seebeck coefficient while the n-type rod has a negative one. Both ends of the rods are joined together by a resistor R_L, which has a colder temperature $T_C < T_H$, illustrated in in Figure 1.

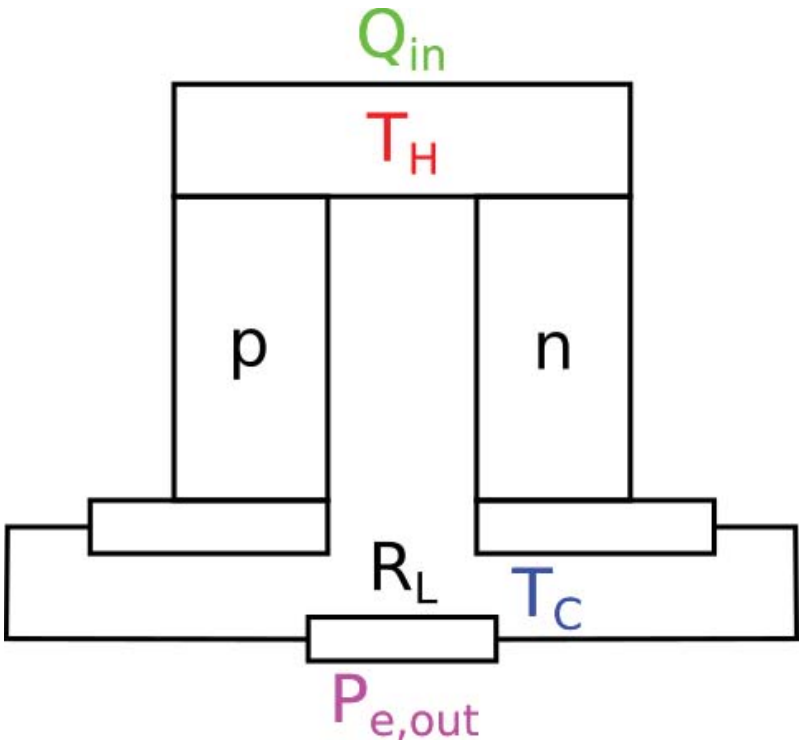

Figure 1: Schematic drawing of a thermoelement.

The Seebeck effect is commonly used to convert heat into electricity and its coefficient is defined by the quotient of the measured voltage ΔV over the applied temperature difference ΔT, seen in Equation 2.2. The opposite conversion is achieved through the Peltier effect, which converts electricity into heat. The Peltier coefficient Π is defined as the amount of the generated heat flux $\dot{Q}$ over the applied current I and is related to the Seebeck coefficient, as is written in Equation 2.3.

$$S = \frac{\Delta V}{\Delta T} \tag{2.2}$$

$$\Pi = \frac{\dot{Q}}{I} = ST \tag{2.3}$$

The overall efficiency of the thermoelement is given by the ratio between the input heat rate $\dot{Q}_{in}$ and the electrical power $P_{e,out}$ at the resistor R_L. While the electrical power dissipated in the resistor R_L is given by $I^2 R_L$, the input heat rate $\dot{Q}_{in}$ consists of Peltier heating, conductive heat transfer and joule heating. The heat rate due to the Peltier effect follows directly from Equation 2.3. Fourier's law describes the rate of heat transfer through the rods and is given by

$$\dot{Q} = \kappa \Delta T, \tag{2.4}$$

where κ is the thermal conductivity. Finally, the amount of joule heating in the thermoelement follows from Ohm's law, where half of it passes to the cold junction and the rest to the hot one.

The total efficiency of the thermoelement is given by

$$\eta = \frac{P_{e,out}}{\dot{Q}_{in}} = \frac{I^2 R_L}{SIT_H + \kappa \Delta T - \frac{I^2 r}{2}}, \tag{2.5}$$

where $S = |S_p| + |S_n|$ is the added Seebeck coefficient, $r = r_n + r_p$ is the resistance of the rods and $\kappa = \kappa_n + \kappa_p$ is the thermal conductivity of the rods.

Using Equation 2.2 together with Ohm's law the current I can be written as $I = \frac{S\Delta T}{R_L + r}$. Inserting this into the efficiency η leads to

$$\eta = \frac{\Delta T}{T_H} \frac{\frac{m}{(m+1)}}{1 + \frac{\kappa r}{S^2} \frac{m+1}{T_H} - \frac{\Delta T}{2T_H} \frac{1}{m+1}}, \tag{2.6}$$

with $m = R_L / r$. The efficiency depends only on the temperature of the cold and hot junction, the ratio $Z = \frac{S^2}{\kappa r}$ and the quantity m.

The maximum efficiency is found by setting the derivative of η with respect to m equal to zero and solving it for m. This leads to the final equation for the maximum efficiency of a thermoelement, where $T_M = \frac{T_H+T_C}{2}$. [4–6]

$$m_{opt} = \sqrt{1 + ZT_M} \tag{2.7}$$

$$\eta_{max} = \frac{\Delta T}{T_H} \frac{\sqrt{1 + ZT_M} - 1}{\sqrt{1 + ZT_M} + \frac{T_C}{T_H}} \tag{2.8}$$

Note that the maximum efficiency of a thermoelectric material is determined by the dimensionless thermoelectric figure of merit, which can be written as

$$ZT = \frac{S^2 T}{\kappa \rho}, \tag{2.9}$$

with ρ as the resistivity of the material. The thermal conductivity consists of the electronic part plus the phononic part, hence $\kappa = \kappa_e + \kappa_{ph}$.

In order to maximize ZT, the Seebeck coefficient S must be maximized while ρ and κ are minimized. However, the physical properties are not independent of each other, which makes it difficult to engineer a good thermoelectric material. The phononic thermal conductivity κ_{ph} is the only quantity, which can be changed freely without influencing the others. [7]

2.2 Modeling the dielectric response

To model the electronic behavior in the material two models were combined to the so called Drude-Lorentz model. The Drude model describes the response of a free electron gas in a metal to an applied electric field. Here the electrons in the conduction band collide with the atomic lattice, which determines the resistivity of the material. This collision is described by the introduction of the plasma scattering time τ, which is the average time for an electron between two collisions. The dielectric function follows the Equation

$$\epsilon(\omega) = -\frac{\omega_p^2}{\omega^2 + i\frac{\omega}{\tau}}, \tag{2.10}$$

where ω is the frequency and ω_p is the plasma frequency, a material constant. The plasma frequency ω_p is the natural resonant frequency of the plasma. For $\omega < \omega_p$ materials behave like metals while above ω_p they become transparent.

A quantitative description for optically active phonons is given by the Lorentz model. In this model a carrier is trapped in a harmonic potential and can be excited through an applied electric field. The relaxation is described by a damping force. The corresponding dielectric function can be written as

$$\epsilon(\omega) = \frac{\Delta\epsilon_j \omega_j}{\omega_j^2 - \omega^2 - i\gamma_j\omega}, \tag{2.11}$$

where $\Delta\epsilon_j$ describes the amplitude of the phonon, ω_j is the resonance frequency of the phonon and γ_j is the damping of the phonon.

This leads to the following Equation for the Drude-Lorentz model

$$\epsilon(\omega) = \epsilon_\infty - \frac{\omega_p^2}{\omega^2 + i\frac{\omega}{\tau}} + \sum \frac{\Delta\epsilon_j \omega_j}{\omega_j^2 - \omega^2 - i\gamma_j\omega}, \tag{2.12}$$

which describes multiple phonons. The constant ϵ_∞ takes the response of the tightly bound core electrons into account. To calculate the reflectivity $R(\omega)$ the following Equation

$$R(\omega) = \left| \frac{1 - \sqrt{\epsilon(\omega)}}{1 + \sqrt{\epsilon(\omega)}} \right|^2 \tag{2.13}$$

is applied.

3 Method

3.1 Experimental setup

The measurements were carried out with a Bruker VERTEX 80v, a Fourier-transform infrared (FTIR) spectrometer, which can be seen in Figure 2. It consists of a vacuum chamber (evacuated to roughly 2 hPa), a light source, a beamsplitter, a polarizer and a detector. The spectrometer operates under a vacuum to reduce the parasitic absorption of H_2O molecules in the air.

Figure 2: Picture of Bruker VERTEX 80v

In order to measure the broadband response of the sample, different light sources, beamsplitters, polarizers and detectors must be used. This is due to the fact that the different optical elements are optimized to work in different optical domains. An overview of the utilized settings can be seen in Table 1.

setting	spectral range [cm^{-1}]	source	beamsplitter	detector
NIR	6000 - 15000 [cm^{-1}]	tungsten lamp	CaF_2	silicon diode
MIR	600 - 6000 [cm^{-1}]	glowbar	KBr	MCT
FIR	50 - 600 [cm^{-1}]	mercury lamp	Mylar 6 μm	bolometer

Table 1: Settings used to measure the broadband response of the samples.

Figure 3 illustrates the beam path of the spectrometer. The electronics were controlled with the software OPUS from Bruker, which also carried out the Fourier transformation of the recorded interferograms. With OPUS the different light sources, beamsplitters (BMS), apertures (APT) and other parameters could be selected and set.

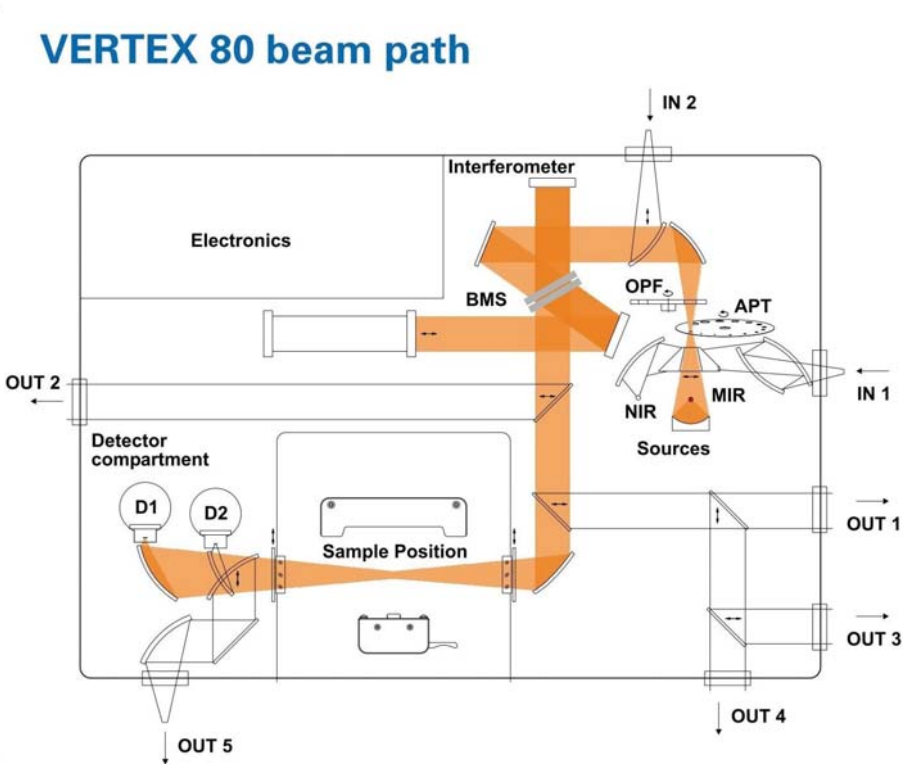

Figure 3: The beam path of Bruker VERTEX 80v from [8].

The mercury lamp, acting as a FIR source was the only source mounted outside of the spectrometer and the radiation was directed into the spectrometer through input IN 1. The bolometer detector was also mounted outside the vacuum chamber and received its signal from output OUT 2 after the radiation passed through the sample position. Switching the samples, polarizers and detectors was carried out by hand.

Since the spectra for the near-infrared (NIR), the mid-infrared (MIR) and the far-infrared (FIR) regions are measured with different optical setups, each spectral band must be combined to give the overall broadband response.

3.1.1 Michelson interferometer

In the spectrometer the radiation is emitted from the source, it then travels through the aperture before reaching the Michelson interferometer. The basic Michelson interferometer consists of a light source, a beamsplitter and two mirrors, which can be seen in Figure 4. A beamsplitter divides the beam into two paths and a moving mirror in one path creates a path difference δ between them. This then creates constructive and destructive interference in the intensity of the beam, which is then diverted onto the sample surface. The reflected signal from the sample surface is then picked up by the detector and recorded as an interferogram.

If both mirrors are equidistant from the light source, then the two beams are in phase with each other and interfere constructively. Constructive interference occurs if the path difference is a multiple integer of the wavelength $\delta = n\lambda$. Moving the mirror at constant velocity gives a sinusoidal intensity at the detector. For a monochromatic light source the interferogram $I(\delta)$ is given by Equation 3.1. Extending this to a continuous light source yields Equation 3.2 for the intensity of the interferogram $I(\delta)$. This describes the Fourier transformation of the intensity of the source $I(\bar{\nu})$, hence the name Fourier-transform spectrometer. Therefore the intensity spectrum $I(\bar{\nu})$ can be calculated through a Fourier transformation of the recorded interferogram $I(\delta)$, which can be seen in Equation 3.3. [9, 10]

$$I(\delta) = I(\bar{\nu_0})cos(2\pi\bar{\nu_0}\delta) \tag{3.1}$$

$$I(\delta) = \int_{-\infty}^{\infty} I(\bar{\nu})cos(2\pi\bar{\nu}\delta)d\bar{\nu} \tag{3.2}$$

$$I(\bar{\nu}) = \int_{-\infty}^{\infty} I(\delta)cos(2\pi\bar{\nu}\delta)d\delta \tag{3.3}$$

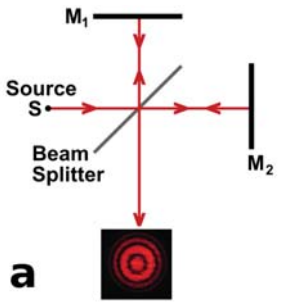

Figure 4: The basics of an Michelson interferometer [11].

3.2 Reflectivity measurements at room temperature

In order to calculate the absolute reflectivity of a sample $R(\nu)$, a gold mirror is commonly used as a reference. The obtained intensity of the sample is given by Equation 3.4, here $R_s(\nu)$ is the reflectivity of the sample and $I_0(\nu)$ is the intensity of the source. For the intensity of the reference Equation 3.5 holds true, since the reference is chosen to have a reflectivity $R_r(\nu)$ of unity. Through the division of the spectrum of the sample with the spectrum of the gold mirror the reflectivity of the sample $R(\nu)$ is obtained, seen in Equation 3.6.

$$I_s(\nu) = R_s(\nu)I_0(\nu) \tag{3.4}$$

$$I_r(\nu) = R_r(\nu)I_0(\nu) = I_0(\nu) \tag{3.5}$$

$$R(\nu) = \frac{R_s(\nu)I_0(\nu)}{R_r(\nu)I_0(\nu)} = R_s(\nu) \tag{3.6}$$

To illustrate this process, the intensity spectra of the sample $Fe_2V_{0.8}W_{0.2}Al$ in the NIR region can be seen in Figure 5.

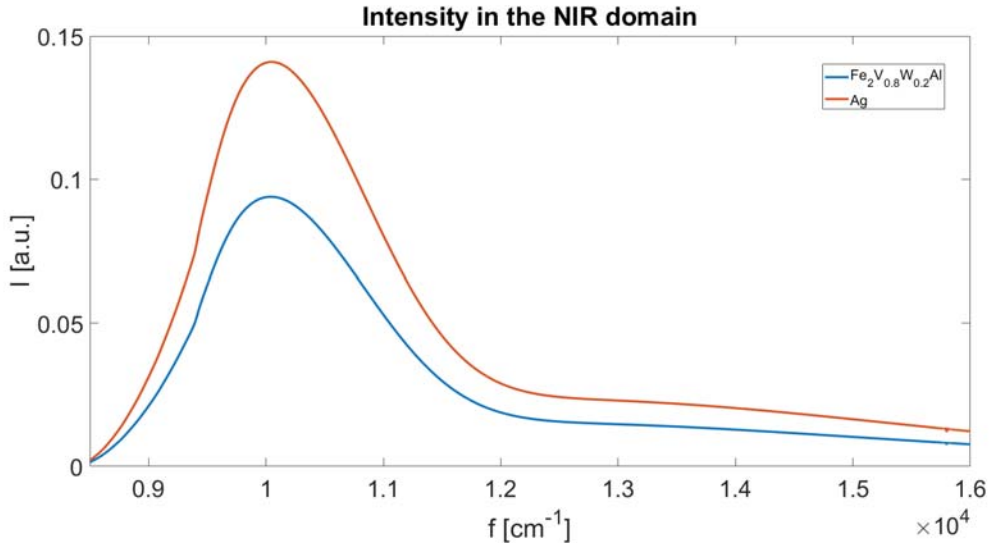

Figure 5: The intensity spectrum of the sample $Fe_2V_{0.8}W_{0.2}Al$ and the gold mirror in the NIR region.

Applying Equation 3.6 onto the measured intensities gives the corresponding reflectivity spectrum of the sample $Fe_2V_{0.8}W_{0.2}Al$ in the NIR region, seen in Figure 6.

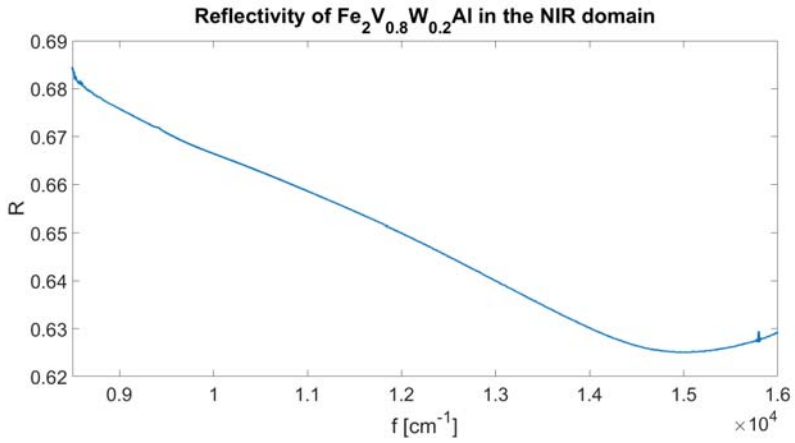

Figure 6: The corresponding reflectivity spectrum of the sample $Fe_2V_{0.8}W_{0.2}Al$ in the NIR region.

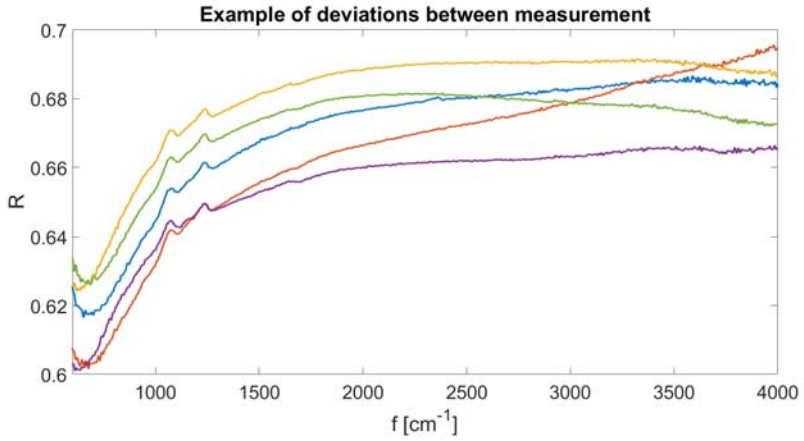

Figure 7: Illustration of the deviations between measurements of Fe_2VAl in the MIR region.

Deviations in the intensity spectrum occurred between single measurements of the sample and the reference, when they were swapped out due to unavoidable modulations in the optical alignment. The corresponding deviations in the reflectivity spectrum of the sample can be seen in Figure 7. In order to get repeatable measurements, multiple measurements were recorded and then averaged.

In between those measurements, the sample and reference were swapped out. Taking the sample or reference out of the holder and reinserting them, causes a small deviation in the beam path of the optical system.

This leads to the observed deviations in the recorded spectra. Therefore multiple measurements had been recorded and then averaged to give a repeatable spectrum of the sample. This averaged reflectivity of the sample Fe_2VAl in the NIR domain can be seen in Figure 8.

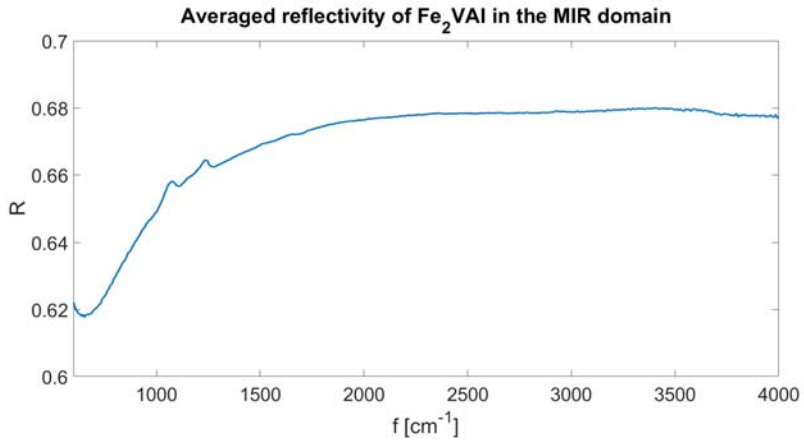

Figure 8: The corresponding averaged reflectivity spectrum of the sample Fe_2VAl in the MIR region.

Finally the individual spectra of each optical domain were combined into the broadband spectra, displayed in Figure 9. Additionally, the optical response of both materials were checked for anisotropy. This was achieved by recording the reflectivity using polarized light with different angles, which can be seen in Figure 10.

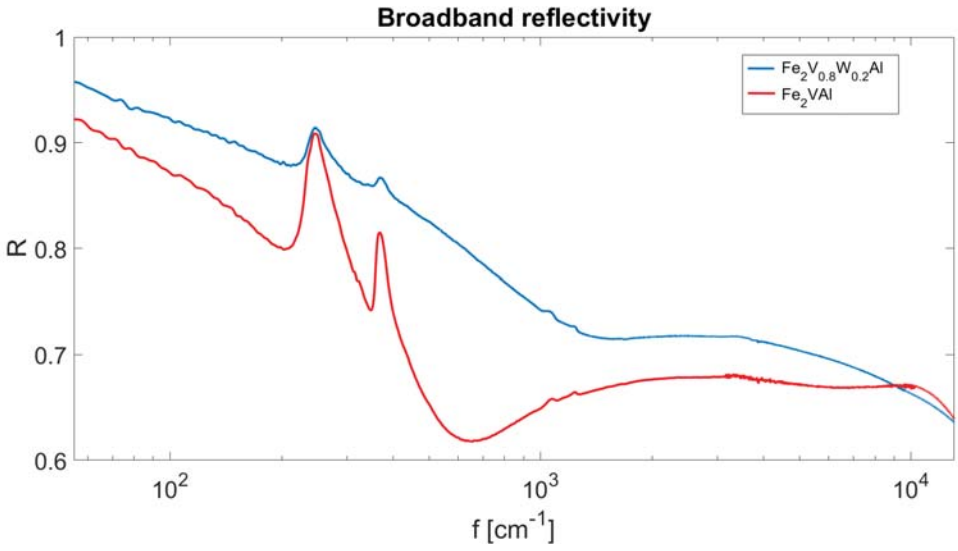

Figure 9: Broadband reflectivity of the two samples.

It can be noted that the deviations in the reflectivity with different polarization angles is in the order of 5%, indicating a mostly isotropic material. The observed anisotropy might be a result of the inhomogeneous surface of the samples.

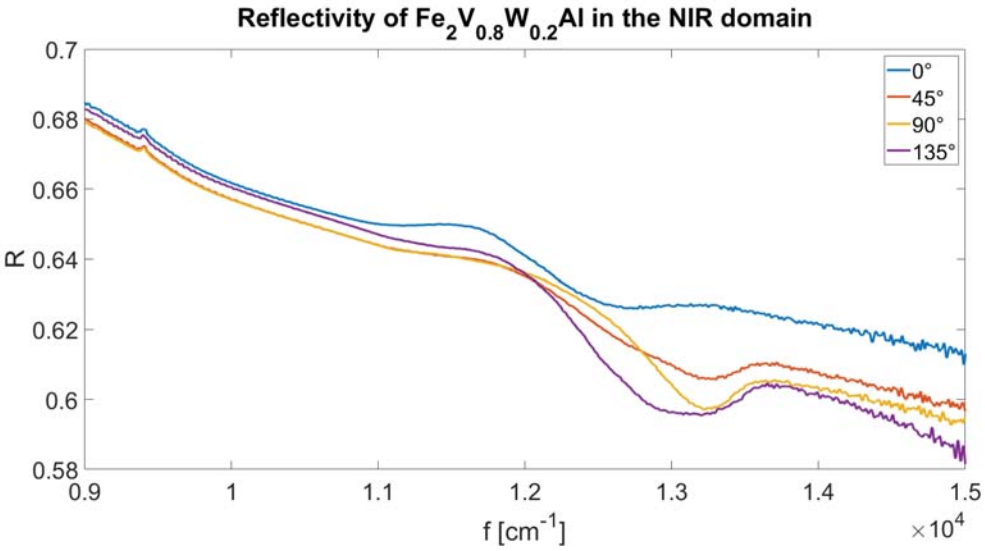

Figure 10: Reflectivity in the FIR region of the sample $Fe_2V_{0.8}W_{0.2}Al$ at different polarization angles.

4 Analysis

The measured broadband reflectivity of Fe_2VAl and $Fe_2V_{0.8}W_{0.2}Al$ show two distinct phonons at roughly 240 cm^{-1} and 366 cm^{-1}, seen in Figure 9. For the V/W substituted material ($Fe_2V_{0.8}W_{0.2}Al$), the phonons seem to be screened and have a broader half-width compared to the nonsubstituted material. All in all the V/W substituted material exhibits a higher reflectivity in general. Comparing the broadband reflectivity of Fe_2VAl with the literature shows a relative good agreement between them, which can be seen in Figure 11.

To analyze the broadband response quantitatively a Drude-Lorentz model was utilized, following the Equation 4.1.

$$\epsilon(\omega) = \epsilon_\infty - \frac{\omega_p^2}{\omega^2 + i\frac{\omega}{\tau}} + \sum \frac{\Delta\epsilon_j \omega_j}{\omega_j^2 - \omega^2 - i\gamma_j\omega} \tag{4.1}$$

The reflectivity data was fitted with a Drude term and 2 to 3 Lorentz oscillators following the Equation

$$R(\omega) = \left| \frac{1 - \sqrt{\epsilon(\omega)}}{1 + \sqrt{\epsilon(\omega)}} \right|^2 \tag{4.2}$$

for the reflectivity. The corresponding fitting Parameters can be seen in Table 2.

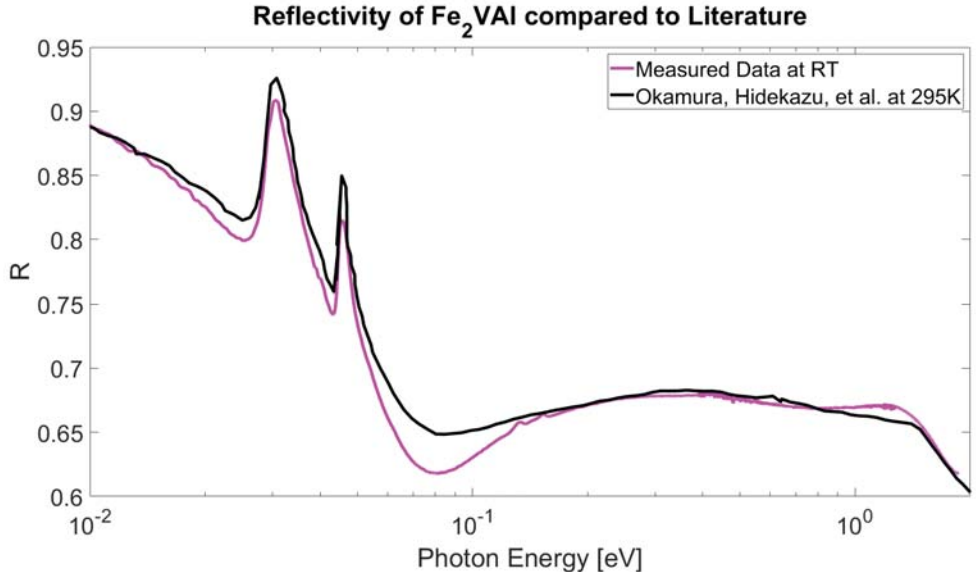

Figure 11: Spectrum of Fe_2VAl compared to Okamura, Hidekazu, et al. "Pseudogap formation in the intermetallic compounds $(Fe_{1-x}V_x)_3Al$". Physical review letters 84.16 (2000).

Fitting parameter	Fe_2VAl 2 Oscillator	Fe_2VWAl 2 Oscillator	Fe_2VAl 3 Oscillator	Fe_2VWAl 3 Oscillator
$\Delta\epsilon_1$	34.14	36.35	30.49	33.22
$\Delta\epsilon_2$	4.995	6.228	4.56	4.65
$\Delta\epsilon_3$	-	-	86.51	155.7
ϵ_∞	104.7	99.26	1	1
τ [cm]	0.001826	0.0003	0.0035	0.00086
ω_1 [cm^{-1}]	240.7	242.4	236.1	241.8
ω_2 [cm^{-1}]	366.1	364.7	363.1	365.5
ω_3 [cm^{-1}]	-	-	2510	39060
ω_p [cm^{-1}]	5246	20430	3778	12330
γ_1 [cm^{-1}]	14.17	17.97	14.17	17.97
γ_2 [cm^{-1}]	18.51	32.78	18.51	32.78
γ_3 [cm^{-1}]	-	-	4531	$3.264 \cdot 10^5$

Table 2: Fitting parameter from the model.

Comparing the two materials with this model, it can be seen, that $Fe_2V_{0.8}W_{0.2}Al$ exhibits a stronger phonon damping γ and a slightly higher phonon amplitude $\Delta\epsilon$. Additionally the plasma frequency ω_p is increased while the Drude scattering time τ is decreased. Since the phonon damping in $Fe_2V_{0.8}W_{0.2}Al$ is increased, the thermal phonon conductivity κ_{ph} of the material should be decreased compared to Fe_2VAl. A decrease in the Drude scattering time τ means, that the conductivity σ is also increased and by that the resistivity ρ decreased. Both of those effects should also increase the thermoelectric figure of merit $ZT{=}\frac{S^2}{\rho\kappa}T$. The decreased resistivity ρ and thermal conductivity κ_{ph} for the V/W substituted material under 300 K was recently shown. [12]

The high ϵ_∞ can be decreased and set to one with the inclusion of a third Lorentz oscillator. This is due to complicated electronic transitions in the region beginning at 1000 cm^{-1}. In Figure 12 the 2 and 3 oscillators fit is illustrated together with the measured data. Including interband transitions in the model improves the fit in the higher frequency region but neglects the dip near 1000 cm^{-1}. This shows the weakness of the currently applied model with 2 or 3 Lorentz oscillators. Therefore the model needs to be improved for these emerging interband transitions. [13, 14]

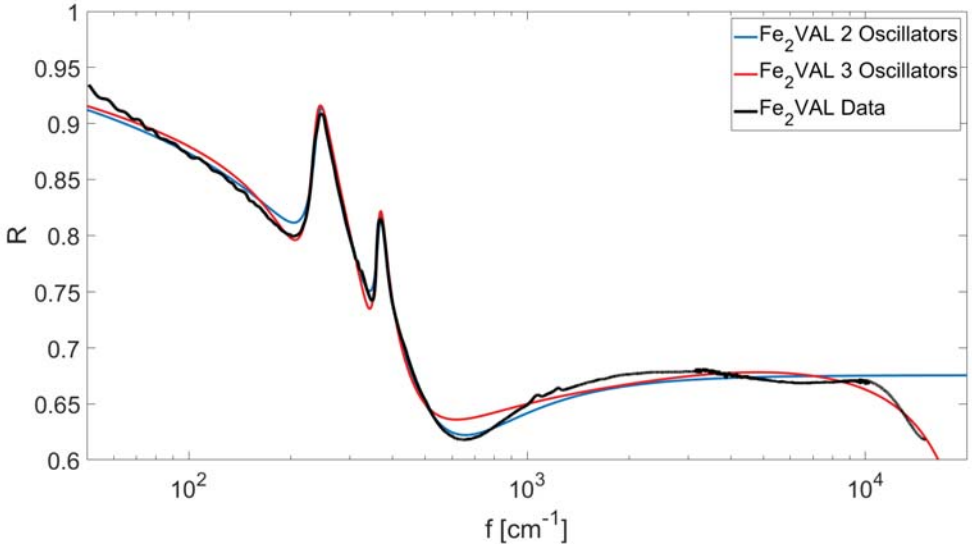

Figure 12: Fitted model of Fe_2VAl with 2 and 3 Lorentz oscillators.

The complex dielectric function $\epsilon(\omega)$ follows directly from this model, which can be seen in Figure 13 and Figure 14. The two observed phonons are clearly visible in the dielectric function. Additional the Kramers-Kronig transformed dielectric function is also included, which was directly calculated from the reflectivity data. It is in a good agreement with the 3 oscillator model and also shows the onset of the interband absorption in the imaginary dielectric function.

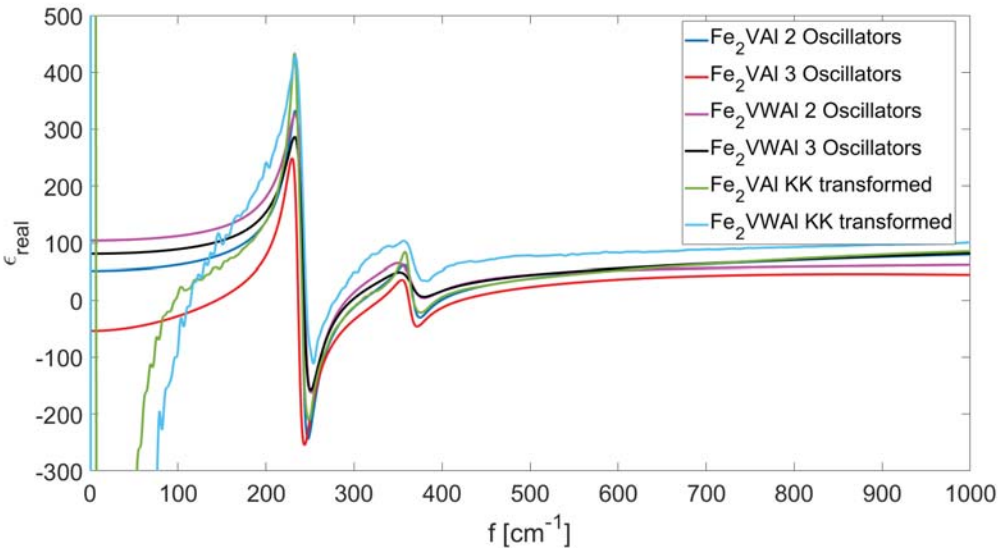

Figure 13: The real part of the dielectric function.

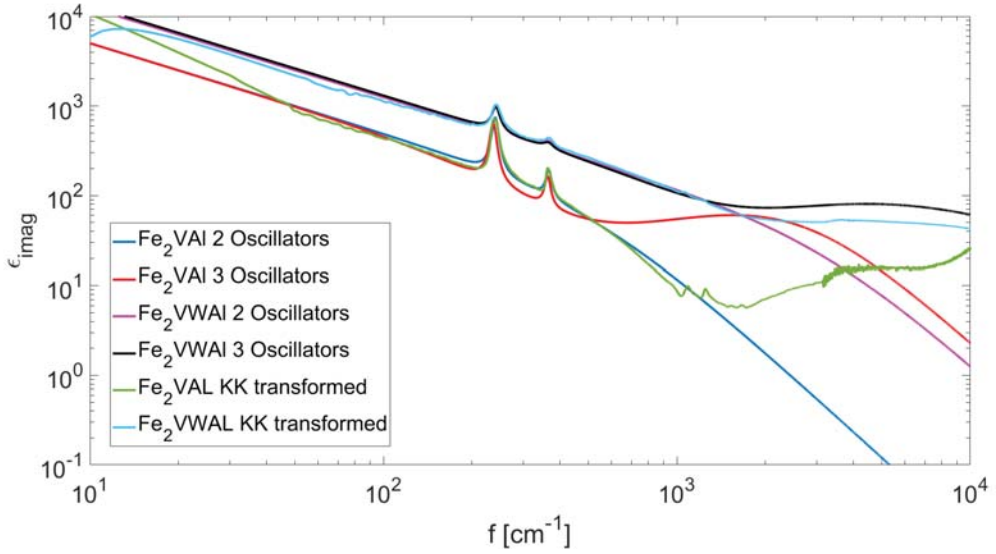

Figure 14: The imaginary part of the dielectric function.

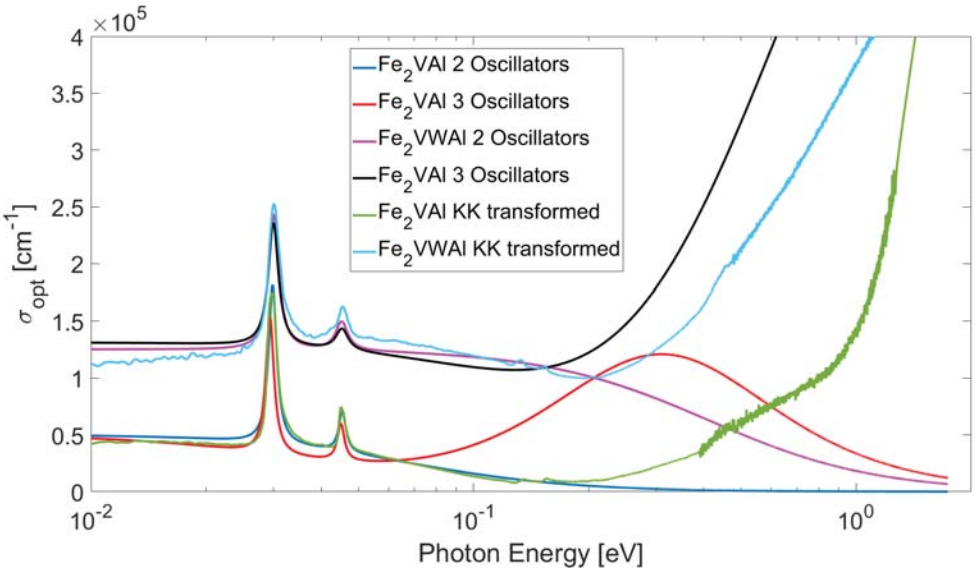

Figure 15: Optical conductivity σ_{opt} plotted for both materials.

From this the optical conductivity was calculated, which can be seen in Figure 15. It also displays the two observed phonons and it can be seen, that the optical conductivity σ_{opt} is higher for $Fe_2V_{0.8}W_{0.2}Al$, which was expected. Comparing the optical conductivity of Fe_2VAl to the literature, reinforces the idea of using a third Lorentz oscillator for the interband transitions peaking at 1.1 eV. [13]

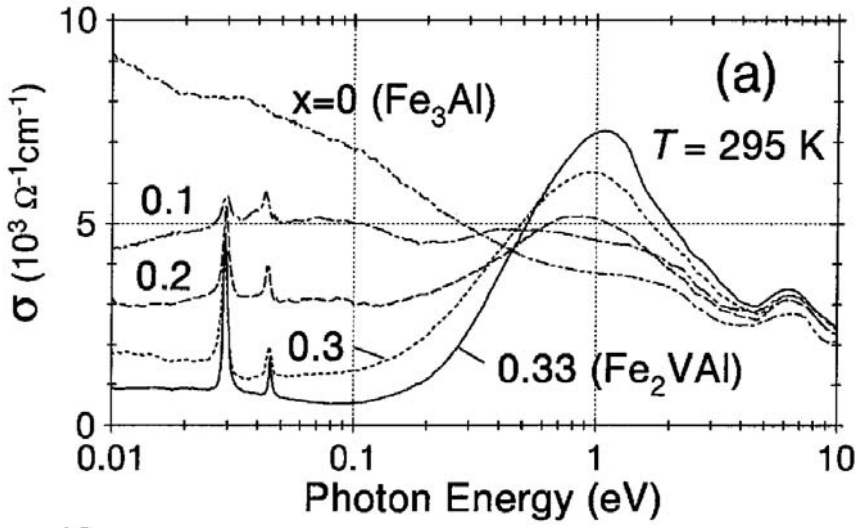

Figure 16: Optical conductivity of Fe_2VAl from Okamura, Hidekazu, et al. "Pseudogap formation in the intermetallic compounds $(Fe_{1-x}V_x)_3Al$". Physical review letters 84.16 (2000).

Improving the model could be done by optimizing the fit for the interband transitions. Alternatively the Kramers-Kronig transformed data could be analyzed for further investigations.

5 Final remarks and outlook

The analysis of the optical response suggests that both the Drude scattering time τ and the thermal phonon conductivity κ_{ph} are decreased in the V/W substituted material $Fe_2V_{0.8}W_{0.2}Al$. The decrease in the Drude scattering time τ decreases the resistivity ρ, which can be seen in the increased optical conductivity σ_{opt}. This suggests an increased thermoelectric figure of merit $ZT = \frac{S^2T}{\rho\kappa}$ for $Fe_2V_{0.8}W_{0.2}Al$.

The model needs to be improved for the higher frequency interband transitions in order to extract the closest fitting dielectric function out of it. This could be achieved by adding additional Lorentz oscillators or going beyond the Drude-Lorentz model.

To characterize the behavior of the thermoelectric transport for these materials the optical response as a function of the W doping should be probed further. The obtained resistivities ρ_x and phononic thermal conductivities $\kappa_{ph,x}$ could give a better understanding of how the V/W substitution influences these properties. This might lead to a new theoretical understanding of these materials and in turn to new ways to engineer more efficient thermoelectric materials in the future. Furthermore probing these properties at low temperature should also be considered for future investigations.

References

[1] M. Mikami, Y. Kinemuchi, K. Ozaki, Y. Terazawa, and T. Takeuchi, "Thermoelectric properties of tungsten-substituted Heusler Fe_2VAl alloy," *Journal of Applied Physics*, vol. 111, no. 9, p. 093710, 2012.

[2] B. Hinterleitner, I. Knapp, M. Poneder, Y. Shi, H. Müller, G. Eguchi, C. Eisenmenger-Sittner, M. Stöger-Pollach, Y. Kakefuda, N. Kawamoto, Q. Guo, T. Baba, T. Mori, S. Ullah, X.-Q. Chen, and E. Bauer, "Thermoelectric performance of a metastable thin-film Heusler alloy," *Nature*, vol. 576, no. 7785, pp. 85–90, 2019.

[3] S. Twaha, J. Zhu, Y. Yan, and B. Li, "A comprehensive review of thermoelectric technology: Materials, applications, modelling and performance improvement," *Renewable and sustainable energy reviews*, vol. 65, pp. 698–726, 2016.

[4] A. F. Ioffe, L. Stil'Bans, E. Iordanishvili, T. Stavitskaya, A. Gelbtuch, and G. Vineyard, *Semiconductor thermoelements and thermoelectric cooling*. Infosearch, ltd., London, 1957.

[5] C. Hapenciuc, T. Borca-Tasciuc, and I. Mihailescu, "The relationship between the thermoelectric generator efficiency and the device engineering figure of merit $Z_{d,eng}$. The maximum efficiency η_{max}," *AIP Advances*, vol. 7, no. 4, p. 045007, 2017.

[6] G. S. Nolas, J. Sharp, and J. Goldsmid, *Thermoelectrics: basic principles and new materials developments*, vol. 45. Springer Science & Business Media, 2013.

[7] J. He, M. G. Kanatzidis, and V. P. Dravid, "High performance bulk thermoelectrics via a panoscopic approach," *Materials Today*, vol. 16, no. 5, pp. 166–176, 2013.

[8] Bruker, "VERTEXseries Brochure EN." `https://www.bruker.com/fileadmin/user_upload/8-PDF-Docs/OpticalSpectrospcopy/FT-IR/VERTEX/Brochures/VERTEXseries_Brochure_EN.pdf`, 2018. Accessed November 22, 2020.

[9] W. Demtröder, *Experimentalphysik*, vol. 2. Springer, 2013.

[10] P. R. Griffiths and J. A. De Haseth, *Fourier transform infrared spectrometry*. John Wiley & Sons, 2007.

[11] FL0, "Formation of fringes in a Michelson interferometer." `https://ru.wikipedia.org/wiki/%D0%98%D0%BD%D1%82%D0%B5%D1%80%D1%84%D0%B5%D1%80%D0%BE%D0%BC%D0%B5%D1%82%D1%80_%D0%9C%D0%B0%D0%B9%D0%BA%D0%B5%D0%BB%D1%8C%D1%81%D0%BE%D0%BD%D0%B0#/media/%D0%A4%D0%B0%D0%B9%D0%BB:Michelson_interferometer_fringe_formation.svg`, 2012. Accessed December 22, 2020.

[12] B. Hinterleitner, P. Fuchs, J. Rehak, F. Garmroudi, M. Parzer, M. Waas, R. Svagera, S. Steiner, M. Kishimoto, R. Moser, R. Podloucky, and E. Bauer, "Stoichiometric and off-stoichiometric full Heusler $Fe_2V_{1-x}W_xAl$ thermoelectric systems," *Physical Review B*, vol. 102, no. 7, p. 075117, 2020.

[13] Y. Feng, J. Rhee, T. Wiener, D. W. Lynch, B. Hubbard, A. Sievers, D. L. Schlagel, T. A. Lograsso, and L. Miller, "Physical properties of Heusler-like Fe_2VAl," *Physical Review B*, vol. 63, no. 16, p. 165109, 2001.

[14] H. Okamura, J. Kawahara, T. Nanba, S. Kimura, K. Soda, U. Mizutani, Y. Nishino, M. Kato, I. Shimoyama, H. Miura, K. Fukui, K. Nakagawa, H. Nakagawa, and T. Kinoshita, "Pseudogap formation in the intermetallic compounds $(Fe_{1-x}V_x)_3Al$," *Physical review letters*, vol. 84, no. 16, p. 3674, 2000.